



LAWRENCE  
LIVERMORE  
NATIONAL  
LABORATORY

# In Situ Grain Fracture Mechanics During Uniaxial Compaction of Granular Solids

R. C. Hurley, D. C. Pagan , J. Lind, M. C. Akin, E.  
B. Herbold

September 17, 2017

Journal of the Mechanics and Physics of Solids

## **Disclaimer**

---

This document was prepared as an account of work sponsored by an agency of the United States government. Neither the United States government nor Lawrence Livermore National Security, LLC, nor any of their employees makes any warranty, expressed or implied, or assumes any legal liability or responsibility for the accuracy, completeness, or usefulness of any information, apparatus, product, or process disclosed, or represents that its use would not infringe privately owned rights. Reference herein to any specific commercial product, process, or service by trade name, trademark, manufacturer, or otherwise does not necessarily constitute or imply its endorsement, recommendation, or favoring by the United States government or Lawrence Livermore National Security, LLC. The views and opinions of authors expressed herein do not necessarily state or reflect those of the United States government or Lawrence Livermore National Security, LLC, and shall not be used for advertising or product endorsement purposes.

# *In Situ* Grain Fracture Mechanics During Uniaxial Compaction of Granular Solids

R. C. Hurley<sup>a,c</sup>, J. Lind<sup>a</sup>, D. C. Pagan<sup>b</sup>, M. C. Akin<sup>a</sup>, E. B. Herbold<sup>a</sup>

<sup>a</sup>*Lawrence Livermore National Laboratory, Livermore, CA 94550, USA*

<sup>b</sup>*Cornell High Energy Synchrotron Source, Ithaca, NY 14853, USA*

<sup>c</sup>*Johns Hopkins University, Baltimore, MD 21218, USA*

---

## Abstract

Grain fracture and crushing are known to influence the macroscopic mechanical behavior of granular materials and be influenced by factors such as grain composition, morphology, and microstructure. In this paper, we investigate grain fracture and crushing by combining synchrotron x-ray computed tomography and three-dimensional x-ray diffraction to study two granular samples undergoing uniaxial compaction. Our measurements provide details of grain kinematics, contacts, average intra-granular stresses, inter-particle forces, and intra-grain crystal and fracture plane orientations. Our analyses elucidate the complex nature of fracture and crushing, showing that: (1) the average stress states of grains prior to fracture vary widely in their relation to global and local trends; (2) fractured grains experience inter-particle forces and stored energies that are statistically higher than intact grains prior to fracture; (3) fracture plane orientations are primarily controlled by average intra-granular stress and contact fabric rather than the orientation of the crystal lattice; (4) the creation of new surfaces during fracture accounts for a very small portion of the energy dissipated during compaction; (5) mixing brittle and ductile grain materials alters the grain-scale fracture response. The results highlight an application of combined x-ray measurements for non-destructive *in situ* analysis of granular solids and provide details about grain fracture that have important implications for theory and modeling.

*Keywords:*

---

---

*Email address:* rhurley6@jhu.edu (R. C. Hurley)

## 1. Introduction

Grain fracture and crushing, also referred to as *breakage*, plays an important role in the mechanical properties of granular materials. These phenomena occur in a variety of engineering applications and geological settings including in earth dams [1], pile driving [2], railway ballasts [3], rapid penetration [4], in shearing of granular fault gouge [5], and in loading of rock masses during geological processes [6]. Because fracture and crushing modify the grain-size distribution, grain angularity, and achievable porosities in granular materials, they play an important role in constraining the mathematical formulation describing the inelasticity of these materials (e.g., see [7, 8, 9]). For example, several studies (e.g., [7, 10, 11]) have linked the onset of macroscopic yielding in soil specimens to the onset of grain breakage, highlighting the importance of understanding grain breakage mechanisms for predicting the onset of plastic behavior. Several studies (e.g., [12, 9]) have linked parameters from critical state soil mechanics to the evolution of grain-size distribution after breakage begins, highlighting the importance of understanding grains comminution for the development of plasticity laws describing post-yield behavior. In addition to providing insight into the applicability of plasticity laws, a precise understanding of *in situ* grain breakage mechanisms may aid in assessing the stress history of geologic soil and rock formations [6].

A variety of grain-scale factors have been linked through experiments, theory, and modeling to fracture and crushing in granular materials. These factors include grain composition (mineralogy and crystal lattice orientation), grain morphology, intra-granular stress, inter-particle forces, and coordination number. In the present paper, we focus on the influence of the orientation of the crystal lattice, intra-granular stress, and inter-particle forces on the breakage process, shedding light on grain breakage mechanisms and the orientation of fracture planes using *in situ* measurements. Before describing our analyses and results, we first provide a brief survey of past research on these topics.

Weibull [13] first postulated a link between breakage and material composition by formulating a “survival probability” for brittle materials that is a function of local tensile strength variability. This variability is captured in a scalar quantity called the Weibull modulus, which varies with grain composition, decreasing as variability in local tensile strength increases. The use of Weibull statistics and moduli to predict and interpret data on fracture and

crushing in granular materials has been widely and successfully adopted (e.g. [7, 10, 14, 15, 16]). Mineralogy and the orientation of the crystal lattice have also been found to influence the nature of crack branching in a variety of materials found in geological formations [17, 18]. Despite the prevalence of numerical models and constitutive laws accounting for anisotropic plasticity and fracture (e.g., [19, 20]), there has been no rigorous assessment of when these models are applicable to *in situ* grain-scale fracture.

Jaeger [21] established the interrelated importance of intra-granular stress and coordination number on fracture behavior by showing that peak intra-granular tensile stress decreases in circular grains as coordination number increases. McDowell and colleagues [7] have incorporated this finding into theories of fracture likelihood by reformulating Weibull’s “survival probability” to explicitly incorporate the coordination number. These authors further argued that the influence of coordination number on fracture must dominate over the influence of factors such as particle shape in order to obtain the fractal distribution of particle sizes widely observed in comminuted soils. Ben-Nun and Einav [22] developed a separate analytical model for grain fracture that supports Jaeger’s findings, exhibiting a reduced likelihood of fracture as coordination number increases. Turner and colleagues [23] used finite-element simulations to confirm the finding that increasing coordination number decreases maximum tensile stress. However, Cil and colleagues [24] found that contact number was not the main predictor of particle fracture in a sample of silica sand under 1D compression.

Russell and colleagues [25] proposed a failure criterion for grains in which rupture occurs when the maximum contact force on a grain reaches a threshold that is independent of other contact forces. de Bono and McDowell [26] showed that, among a variety of fracture criteria incorporating major principal stress, mean stress, and maximum inter-particle force, only the criterion incorporating maximum inter-particle force produces behavior observed in experiments and simulations. Karatza and colleagues [27] used simulations and tomographic images to show that the spatial concentration of particle breakage appears correlated with the spatial concentration of the largest inter-particle normal forces. However, the inference of inter-particle forces in stiff 3D packings has only recently become achievable [28], and a thorough investigation of *in situ* fracture has not yet employed this capability.

The studies described above have highlighted the complex interplay of various grain-scale factors in the breakage mechanics of grains. They have also illustrated the need for further research to clarify the relative importance

of these factors in different loading environments and for different granular materials. The studies involved a variety of numerical and experimental approaches. Experimental compression of individual, or small groups of, grains compressed between two or more objects, with post-mortem analysis of grain fragments, has been widely used to investigate fracture behavior (e.g., [21, 15, 29, 16, 30]). The advent of x-ray computed tomography has recently permitted detailed *in situ* and post-mortem studies of the spatial concentration of grain breakage and of grain fragment sizes (e.g., [27, 29, 31]). Finite Element (FE) and Discrete Element Method (DEM) simulations have been employed to investigate the conditions under which single or several grains break *in situ* during a variety of loading conditions (e.g., [23, 24, 5, 16, 32]).

In this paper, we investigate *in situ* grain fracture and crushing in two samples of granular material subjected to uniaxial compaction with combined synchrotron x-ray computed tomography (XRCT) and three-dimensional x-ray diffraction (3DXRD), also called far-field high-energy diffraction microscopy (ff-HEDM). When combined, these two x-ray measurements permit concurrent evaluation of grain kinematics, contacts, local strains and porosities, average intra-granular stresses, inter-particle forces, and crystal and fracture plane orientations [28, 33]. Prior research has demonstrated the utility of XRCT for investigating grain-scale mechanics [27, 34] and the combined use of XRCT and 3DXRD for studying stress concentrations, fracture, grain kinematics, and forces [35, 36, 28, 33, 37, 38]. In the present study, we combine XRCT and 3DXRD in order to determine how the orientation of intra-grain crystal lattices, intra-granular stresses, and inter-particle forces influence the presence and nature of intra-granular fractures. We use a sample with spherical sapphire grains to investigate effects of boundary layers between different sizes and packing and system size effects [33], and a sample with sapphire grains mixed with copper grains to observe the influence of large contact areas and a secondary ductile phase.

The paper is arranged as follows. In Section 2, we describe the experimental methods and data analyses associated with the x-ray measurements. In Section 3, we describe the two uniaxial compaction experiments that are the focus of the paper. Also as part of this section, we describe intra-granular fractures and their mechanisms of formation using the analyses from Section 2. In Section 4, we provide a discussion of the implications of our work and future directions, and in Section 5 we provide concluding remarks.

## 2. Experimental Methods and Analyses

Two granular samples were studied in this work. The first sample contained 989 spherical single-crystal sapphire grains, 549 with diameter  $193 \pm 2 \mu\text{m}$  and 440 with diameter  $155 \pm 4 \mu\text{m}$ , and was described previously in [33]. The second sample contained 205 spherical single-crystal sapphire grains, 95 with diameter  $193 \pm 2 \mu\text{m}$  and 110 with diameter  $158 \pm 4 \mu\text{m}$ , and 28 copper grains, which passed a #50 mesh screen (0.3 mm) and were retained on a #70 mesh screen (0.212 mm). Both samples were prepared by alternating the pouring of grains with different sizes or compositions into a 10 mm tall Al-6061 cylinder with inner diameter 1.5 mm. Prior to preparation, a steel platen with diameter 1.5 mm was inserted into the bottom 5 mm of the cylinder. After preparation, the platen and cylinder were placed in the compact load frame [39] present at the 1-ID-E hutch of the Advanced Photon Source (APS) at Argonne National Laboratory. The samples were loaded in uniaxial compression by lowering a 1.5 mm steel piston into the top of the cylinder and recording the force transmitted through the sample with a load cell below the bottom platen.

Figure 1(a) shows a schematic of the compact load frame and conditions present at the 1-ID-E hutch of APS during the experiment. In both experiments, applied load was increased by lowering the top piston at a constant velocity of approximately  $1 \mu\text{m/s}$  until a desired load cell reading was reached. The piston position was then held constant as 1 mm tall volumes of the sample were illuminated by a 51.996 keV monochromatic x-ray beam. During sample illumination, the sample was rotated twice through  $360^\circ$ , skipping  $40^\circ$  sections on opposite sides of the sample due to x-ray blockages from the compact load frame's support posts. During the first  $180^\circ$  of the first full rotation, a Retiga 4000 CCD camera with  $2048 \times 2048$  pixels, a 10x objective, and a  $0.47 \mu\text{m}$  effective pixel resolution captured transmission radiographs at  $0.25^\circ$  increments. During the second full rotation, a GE-41RT area detector with  $2048 \times 2048$  pixels captured diffraction peaks at  $0.25^\circ$  increments at all angles not blocked by support posts. The load steps at which these rotations and x-ray measurements took place are shown in the loading curves of Figs. 1(d) and 1(e) for the first and second samples, respectively. For the first sample, uniaxial compaction proceeded until softening was observed in the load-displacement curve. A single unload-reload cycle was performed during compaction but will not be analyzed further here. For the second sample, uniaxial compaction proceeded until widespread grain fracture was

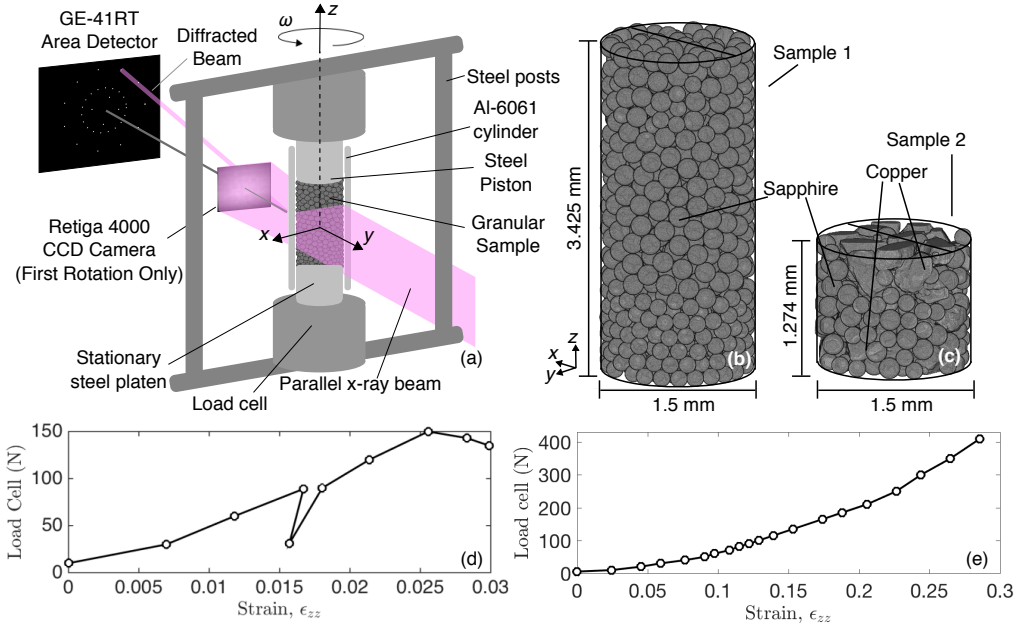


Figure 1: (a) Schematic of the experimental setup at APS, showing relevant features of the compact load frame and image acquisition systems. (b) XRCT reconstruction for the first sample. (c) XRCT reconstruction for the second sample. (d) Load-strain curve for the first sample. (e) Load-strain curve for the second sample.

evident in transmission radiographs and significant strain was achieved. In the remainder of this section, we describe our analyses and refinement of these data for calculating grain centroids, contacts, volume-averaged grain stresses, inter-particle forces, crystal plane orientation, and fracture plane orientations. Some of this information is also provided in [33], but is repeated here for completeness.

### 2.1. XRCT Analysis for Grain Attributes, Contacts

XRCT reconstructions were generated for each granular sample using inverse radon transforms in Matlab<sup>®</sup>. Resulting reconstructions had a voxel size of  $0.74 \mu\text{m}$  but were down-sampled to images with a voxel size of  $4.44 \mu\text{m}$  for most of the analysis described here to improve processing performance. These images were further processed in Matlab<sup>®</sup> using morphological operations such as opening, closing, watershed, and connected components, to segment individual grains. Figures 1b and 1c show the reconstructions for the first and second samples analyzed in this study, respectively. Grain vol-



umes were calculated by summing the number of voxels belonging to each grain and centers of mass were calculated by taking the unweighted average of voxel positions belonging to each grain.

Inter-particle contacts were determined by analyzing labeled XRCT reconstructions in which each grain or object (including the aluminum tube and steel platen and piston) was represented by voxels with a unique integer value. As described in [33], a contact search was performed by moving a 26-voxel neighborhood around each voxel in the image and adding voxels to ID-pair lists if their 26-voxel neighborhood contained two IDs. A collection of voxels for a given ID-pair was deemed a contact if the list contained approximately 0.02% of the grain’s volume. Contacts between touching copper grains and between copper grains and all boundaries were not tracked. The eigenvalues and eigenvectors of the covariance matrix for each contact, corresponding to the positions of each voxel minus the mean position for all voxels belonging to that contact, was used to determine the normal vector (the minor direction) and a basis for the tangent plane (the major and intermediate direction). Normal vectors and tangent plane basis vectors were used in subsequent calculations of inter-particle forces and fabric tensors for each grain. The fabric tensor was computed for each grain by

$$F_{ij} = \sum_{c=1}^{N_c} n_i^c n_j^c, \quad (1)$$

where subscripts indicate tensor indices,  $N_c$  is the number of contacts for the grain and  $n_i^c$  is the normal vector for contact  $c$ . In computing  $F_{ij}$  for each sapphire grain, we consider all sapphire-sapphire contacts, sapphire-boundary contacts, and sapphire-copper contacts (for the second sample). The location and normal vector of sapphire-copper contacts is described next.

For sapphire-copper contacts in the second sample, contact area was computed by first assuming the sapphire grains were spheres and then performing a Lambert azimuthal equal-area projection of contact voxels [40]. This projection maps points on the surface of a sphere to surface of a disk of radius 2, on which equal areas on the disk correspond to proportional equal areas on the surface of the sphere. The area of the convex hull of the resulting points was then used to compute the contact area,  $A_c$ , between the sapphire and copper by  $A_c = A_p 4\pi R_i^2 / (\pi R_d^2)$ , where  $A_p$  is the area of the convex hull of projected points,  $R_i$  is the grain radius, and  $R_d = 2$  is the radius of the disk onto which the project maps points. The location of the sapphire-copper

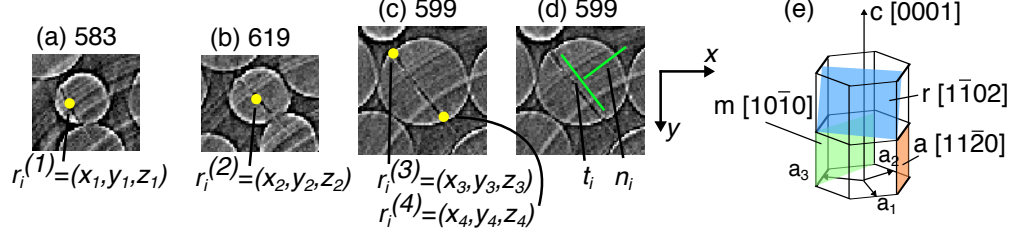


Figure 2: Example of fracture plane identification by using two points in different slices (a,b) and two points in the same slice (c,d) to form a basis for a planar fracture surface. The coordinate axes next to (d) applies to all slices (a)-(d). The coordinate system for the XRCT images is right-handed, but appears left-handed from the coordinate axes because the slices are rendered with positive  $z$  pointing into the page. (e) A simple schematic of the trigonal crystal structure of single-crystal sapphire and relevant families of crystal planes.

contact surface was assumed to be the closest point on the surface of the sapphire grain to the mean location of the contact voxels, and the normal vector of the contact was assumed to be parallel to a line connecting that location to the centroid of the sapphire grain.

## 2.2. XRCT Analyses for Fracture Plane Orientations

Fracture plane orientations were used to analyze resolved shear and normal stress within grains that fractured and for comparison with crystal plane orientations having known fracture toughnesses. Fracture plane orientations were determined manually from XRCT images as follows. First, fractured grains were identified in a given load step by studying XRCT images and 3DXRD data. This process can be automated in future work, but the XRCT reconstructions used in this work were not of sufficient quality to permit locating fractures using an automated algorithm. Once a fracture plane was identified, two points on the primary fracture surface in a grain were identified in two separate slices in the  $x$ - $y$  plane, and two additional points were identified in a single slice in the  $x$ - $y$  plane. Figures 2(a) and 2(b) illustrate the two points identified in two different slices, 583 and 599, for a specific grain. These slices were chosen toward the bottom and top of the fracture, respectively. Figure 2(c) illustrates the two additional points identified in a single slice for the same grain. This slice, 599, was chosen to fall between the two other slices and approximately at the position at which the fracture's length was the greatest.

With the four points identified from XRCT images, two vectors falling approximately on the fracture surface were calculated as

$$v_i^{(1)} = r_i^{(1)} - r_i^{(2)}; \quad v_i^{(2)} = r_i^{(3)} - r_i^{(4)}. \quad (2)$$

Writing the normalized vectors as  $\tilde{v}_i^{(1)}$  and  $\tilde{v}_i^{(2)}$ , a vector normal to the fracture surface is

$$n_i = \epsilon_{ijk} \tilde{v}_j^{(1)} \tilde{v}_k^{(2)}, \quad (3)$$

where  $\epsilon_{ijk}$  is the Levi-Civita symbol and Eqn. (3) therefore represents a cross product between  $\tilde{v}_j^{(1)}$  and  $\tilde{v}_k^{(2)}$ . The normalized form of  $n_i$  is written as  $\tilde{n}_i$ . A set of basis vectors for the fracture plane can then be written as

$$\tilde{t}_i^{(1)} = \tilde{v}_i^{(1)}; \quad \tilde{t}_i^{(2)} = \epsilon_{ijk} \tilde{v}_j^{(1)} \tilde{n}_k^{(1)}. \quad (4)$$

Figure 2(d) illustrates the approximate projection of  $\tilde{n}_i$  and  $\tilde{t}_i^{(2)}$  into the  $x$ - $y$  plane.

We note three sources of human bias in the manual identification of fracture surfaces described above. First, human bias was introduced in identifying the primary fracture in grains possessing multiple fracture planes. In selecting a primary fracture surface, we were careful to identify fracture planes that appeared to have the greatest surface area. However, it is not always possible to identify such a fracture plane, as will be clear in figures shown later. Second, human bias was introduced in selecting the points  $r_i^{(1)}, r_i^{(2)}, r_i^{(3)}$ , and  $r_i^{(4)}$ , shown in Fig. 2. The process of identifying these points was repeated twice with a typical difference of vector orientations of no more than  $6^\circ$ . Finally, bias was introduced by using slices in the  $x$ - $y$  plane, rather than any other plane, for identifying points in the fracture plane. This last source of bias is likely minimal because most fractures have high dip angles from the  $z$ -axis and tend to align with principal tensile stress directions, which themselves tend to fall in the  $x$ - $y$  plane. Finally, we note that fracture surfaces are not always planar, but often possess curvature. An example of this curvature is evident by comparing Figs. 2(a) and 2(b). Nevertheless, the procedure for identifying a fracture plane outlined above should produce a first-order estimate of the average fracture orientation.

### 2.3. 3DXRD Analysis for Grain Stresses and Crystal Plane Orientations

The open-source software HEXRD [41] was used for analysis and reduction of diffraction patterns. Diffraction patterns were first imported by the

HEXRD software and the software was then provided with approximate lattice parameters for sapphire. HEXRD was used to associate diffraction peaks with individual single-crystal grains. Restricting consideration only to families of lattice planes whose diffraction rings fell within the extents of the 3DXRD images, grains were retained for strain calculation if the number of observed diffraction spots was at least 60% of expected (a retention threshold of 0.6 in [42]). For the first sample, 828 to 950 grains were retained for strain calculation, depending on the load step. For the second sample, 193 to 202 grains were retained for strain calculation, depending on the load step. Grain stresses were calculated using grain strains and single-crystal elastic moduli values of sapphire [43]:  $C_{11}=502$  GPa,  $C_{12}=161$  GPa,  $C_{13}=125$  GPa,  $C_{14}=-19$  GPa,  $C_{33}=501$  GPa, and  $C_{44}=157$  GPa.

HEXRD was used to identify the orientation of crystal planes within each sapphire grain. Sapphire has trigonal symmetry and belongs to the  $R\bar{3}c$  space group. HEXRD was therefore used to provide orientations of the c-plane, [0001], the six-fold orientations of the r-planes (e.g.,  $[1\bar{1}02]$ ), the three-fold orientations of the a-planes (e.g.,  $[11\bar{2}0]$ ), and the three-fold orientations of the m-planes (e.g.,  $[10\bar{1}0]$ ). A simple schematic of these planes are shown in Fig. 2(e), although more thorough diagrams of sapphire’s crystal structure can be found in [44]. These orientations were used in subsequent analysis, described below, to assess the influence of anisotropic fracture toughness on the orientation of fracture surfaces within each grain.

#### 2.4. XRCT and 3DXRD Analysis for Inter-particle Forces

Following the calculation of grain and contact orientations, and intra-granular stresses, force vectors were inferred at each inter-particle contact using methods described in [28, 33]. Following this procedure, the inferred forces are those that best satisfy equilibrium and volume-averaged stress measurements for each grain, while also enforcing frictional constraints on each force vector. Sapphire-sapphire contacts were assumed to have a friction coefficient of 0.1 and both sapphire-aluminum and sapphire-steel contacts were assumed to have a friction coefficient of 0.4, both of which are approximately consistent with tabulated values [45].

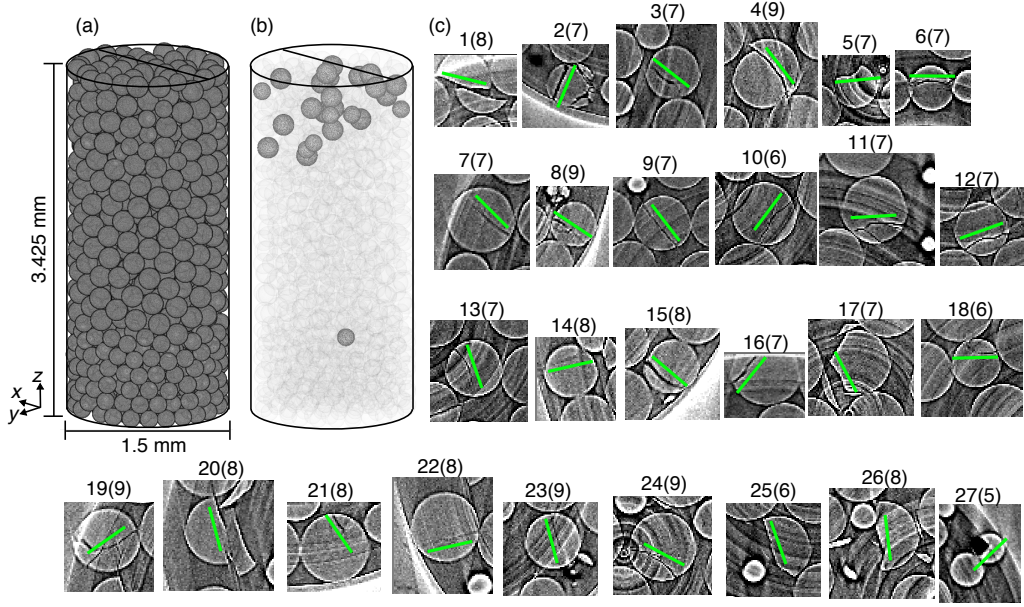


Figure 3: Two renderings of sample 1 at load step 0, (a) showing all grains and (b) highlighting those that fracture during sample compaction. (c) Separate figures of each fractured grain, shown in the  $x$ - $y$  plane, with a green line to guide the reader toward identifying the approximate location of the projection of  $\tilde{t}_i^{(2)}$  into the  $x$ - $y$  plane. Figures are labeled by a grain index and load step (in parentheses) indicating the first load step in which fracture was observed. Lines crossing the entire figures are ring artifacts generated during image reconstruction.

### 3. Findings from Experiments

#### 3.1. Sample 1: Sapphire Spheres During Uniaxial Compaction

During compaction of the first sample, which contained 989 single-crystal sapphire grains, 27 grains fractured between steps 5 and 9. Of the 27 grains that fractured, 8 were of the smaller radius ( $155 \pm 4 \mu\text{m}$ ) and 19 were of the larger radius ( $193 \pm 2 \mu\text{m}$ ). Figure 3 contains two renderings of the sample at load step 0, one showing all grains and one highlighting grains that fractured. A separate snapshot, shown in the  $x$ - $y$  plane, is also presented for each grain at the first step in which fracture was observed. Approximate locations of the projection of  $\tilde{t}_i^{(2)}$  for the primary fracture planes are indicated with a green line.

##### 3.1.1. The influence of intra-granular stress on fracture

We used the average stress tensor for each grain,  $\sigma_{ij}$ , to study the role of intra-granular hydrostatic and distortional stress on fracture. Hydrostatic and distortional, or von Mises, stresses were computed by

$$\sigma_h = \sigma_{ii}/3 \quad \text{and} \quad \sigma_m = \sqrt{((\sigma_1 - \sigma_2)^2 + (\sigma_2 - \sigma_3)^2 + (\sigma_3 - \sigma_1)^2)/2}, \quad (5)$$

respectively, where  $\sigma_{ii}$  is the trace of  $\sigma_{ij}$  and  $\sigma_n$  is the  $n^{\text{th}}$  eigenvalue of  $\sigma_{ij}$ . Figure 4(a) illustrates a density map of the minimum and maximum values of  $\sigma_h$  and  $\sigma_m$ , respectively, for all grains across all load steps. Superimposed on the density map are the trajectories of  $(\sigma_h, \sigma_m)$  in 25 of the 27 grains that fractured. The symbols represent the  $(\sigma_h, \sigma_m)$  states of these grains in the step immediately before ( $S_f - 1$ ) or two steps before ( $S_f - 2$ ) fracture was first observed. These two states were chosen because it is possible that fractures, below the XRCT resolution, occurred in these grains in the step before larger fractures were observed in XRCT images. Grains without the minimum number of diffraction spots required to pass the 3DXRD retention threshold for these steps were not considered. Grains experiencing fracture tend to also experience higher  $\sigma_m$  (average of 171.6 MPa) in the steps immediately prior to fracture, than those reached at any step by all grains (114.3 MPa). A two-sided Welch's  $t$ -test [46] (which compares differences in means between two samples with distinct variances) within the populations of fracturing grains and all grains, confirms that this difference is statistically significant at the 99% confidence level in the present sample (possibly non-integer degrees of freedom computed using the Welch-Satterthwaite formula [47], d.o.f. = 25.4,  $t = 4.3$ ). Grains experiencing fracture also tend to experience a lower

$\sigma_h$  (mean of -67.3 MPa) in the steps immediately prior to fracture, than those reached at any step by all grains (mean of -73.9 MPa). However, this result is not significant according to a Welch's  $t$ -test (d.o.f. = 26.6,  $t = -1.13$ ). The high variance in these both  $\sigma_h$  and  $\sigma_m$  evident in Fig. 4(a) is not surprising when considering the variety of contact states that fracturing grains experience in this sample.

Figures 4(c) and 4(d) show density maps for the large and small grain size populations, respectively, using the same colors as Fig. 4(a) but with 0 and 20 as the colorbar extents. These figures convey minor differences in the spreads of  $(\sigma_h, \sigma_m)$  states for the two grain size populations. Larger grains experience slightly lower average  $\sigma_m$  (169.1 MPa versus 178.0 MPa) and  $\sigma_h$  (-73.9 MPa versus -82.2 MPa) states than small grains prior to fracture. Within the large grain size population,  $\sigma_m$  for fracturing grains remains higher than the general population of grains at the 99% confidence level according to a Welch's  $t$ -test (d.o.f. = 18.2,  $t = 3.12$ ). Within the small grain size population,  $\sigma_m$  for fracturing grains is higher than the general population at the 95% confidence level (d.o.f. = 6.24,  $t = 3.00$ ).

To further explore the role of intra-granular stress on fracture, we used  $\sigma_{ij}$  for each grain with  $\tilde{n}_i, \tilde{t}_i^{(1)}$ , and  $\tilde{t}_2^{(2)}$ , to estimate the resolved normal stress,  $\sigma_n = \sigma_{ij}\tilde{n}_i\tilde{n}_j$ , and shear stress,  $\sigma_t = \sqrt{\sigma_{t1}^2 + \sigma_{t2}^2}$ . For calculating the latter stress,  $\sigma_{t1} = \sigma_{ij}\tilde{n}_j\tilde{t}_i^{(1)}$  and  $\sigma_{t2} = \sigma_{ij}\tilde{n}_j\tilde{t}_i^{(2)}$ , on each grain's primary fracture surface. These quantities only estimate the resolved normal and shear stress on each fracture surface because intra-granular stress fields vary significantly near contact points and significantly larger or smaller stresses are expected in localized areas within each grain.

A means for comparing resolved normal and shear stresses with stresses in grains that do not fracture is not obvious. We chose to compute the maximum and minimum principal stresses,  $\sigma_1$  and  $\sigma_3$ , respectively, and the maximum shear stress,  $\sigma_s = (\sigma_1 - \sigma_3)/2$ , for grains that do not fracture. Density maps of  $(\sigma_3, \sigma_s)$  and  $(\sigma_1, \sigma_s)$  are illustrated on the same plot in Fig. 4(b). Superimposed on the density maps are the trajectories, in  $(\sigma_n, \sigma_t)$  space, of 25 of the 27 grains that fractured. As in Fig. 4(a), symbols in Fig. 4(b) represent states of these grains in the step or two before fracture was first observed. We are not accounting for the rotation of  $\tilde{n}_i, \tilde{t}_i^{(1)}$ , and  $\tilde{t}_2^{(1)}$  in the steps prior to fracture. However, grain rotations are significantly less than  $1^\circ$  on average between load steps in this experiment, less than the fracture plane orientation bias described in section 2.2.

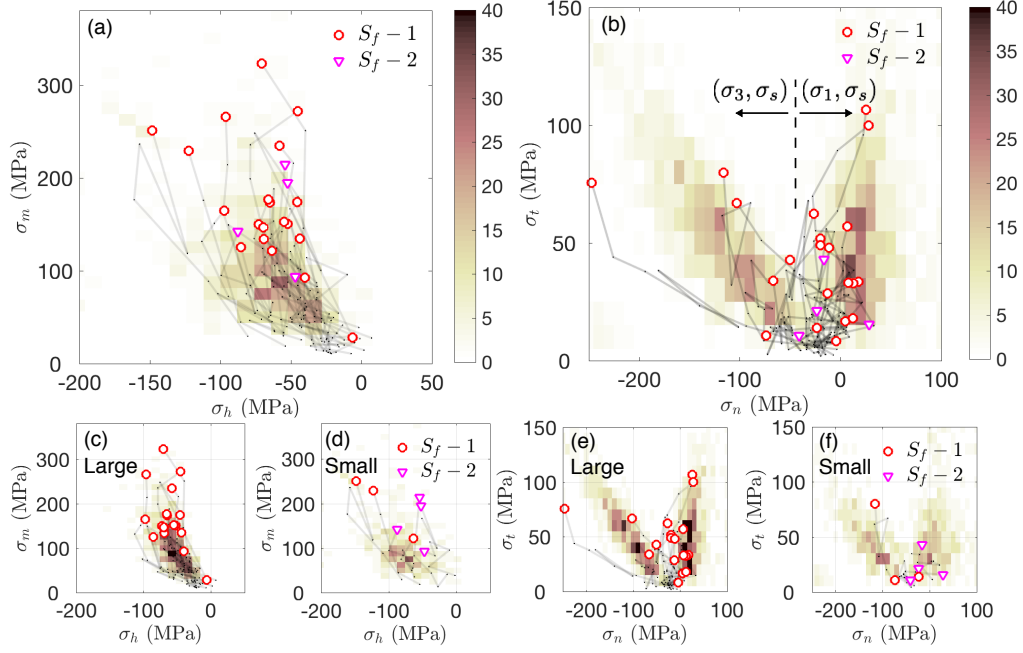


Figure 4: (a) A density map of the minimum and maximum  $(\sigma_h, \sigma_m)$  states for all grains across all load steps, with trajectories of grains that fracture and their state in the steps prior to fracture indicated by symbols.  $S_f - 1$  indicates grains with 3DXRD measurements available in the step immediately prior to fracture, while  $S_f - 2$  indicates grains with 3DXRD measurements available only two steps prior to fracture. (b) Density maps of  $(\sigma_3, \sigma_s)$  and  $(\sigma_1, \sigma_s)$  for each grain, where  $\sigma_3$  is the minimum value achieved at any load step during compaction and  $\sigma_1$  is the maximum value achieved at any load step. Also shown are trajectories of  $(\sigma_n, \sigma_t)$  on the planar primary fracture surface of grains in the steps prior to fracture. (c,d) The same results shown in (a) but for the large (c) or small (d) grain size populations. (e,f) The same results shown in (b) but for the large (e) and small (f) grain size populations.



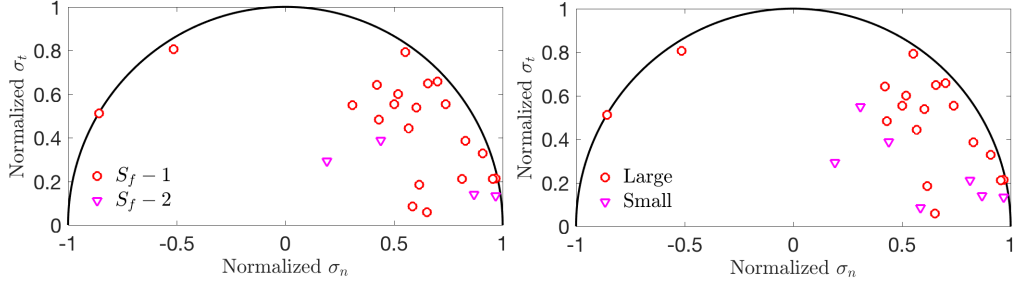


Figure 5: Normalized Mohr's circles showing normalized values of  $\sigma_n$  and  $\sigma_t$  on the planar fracture surface in each grain that fractures, in the step prior to fracture. (a) Mohr's circle dividing grains into  $S_f - 1$  and  $S_f - 2$  populations. (b) Mohr's circle dividing grains into large and small grain size populations.

Grains that experience fracture exhibit widely varying resolved normal and shear stresses on their fracture planes prior to failure. The only observable trend in Fig. 4(b) is that a majority of grains that fracture do so on planes with  $\sigma_n$  closer to the maximum tensile stress in the grain than the maximum compressive stress. In fact, only two grains fracture on planes closer to their maximum compressive stress direction. To corroborate this observation, we normalized  $\sigma_n$  and  $\sigma_t$ , using  $\sigma_1$  and  $\sigma_3$  for each grain, and plotted them together on a single Mohr's circle in Fig. 5(a). To normalize  $\sigma_n$ , we computed

$$\text{Normalized } \sigma_n = \frac{\sigma_n - \sigma_3}{\sigma_1 - \sigma_3}, \quad (6)$$

for each grain. To normalize  $\sigma_t$ , we computed

$$\text{Normalized } \sigma_t = \frac{2\sigma_t}{\sigma_1 - \sigma_3} \quad (7)$$

for each grain. We again observe nearly all fractures to occur along planes more closely aligned with the principal tensile stress than with the principal compressive stress (mean of normalized  $\sigma_n$  is 0.54). This finding is confirmed in later analysis of fracture orientations.

Figures 4(e) and 4(f) illustrate density maps of  $(\sigma_3, \sigma_s)$  and  $(\sigma_1, \sigma_s)$  for the large and small grain size populations, respectively, using the same colors as Fig. 4(b) but with 0 and 20 as the colorbar extents. As in Figs. 4(c) and 4(d), these maps convey a difference in behavior between the two grain size populations. The most notable observation is that small grains experiencing

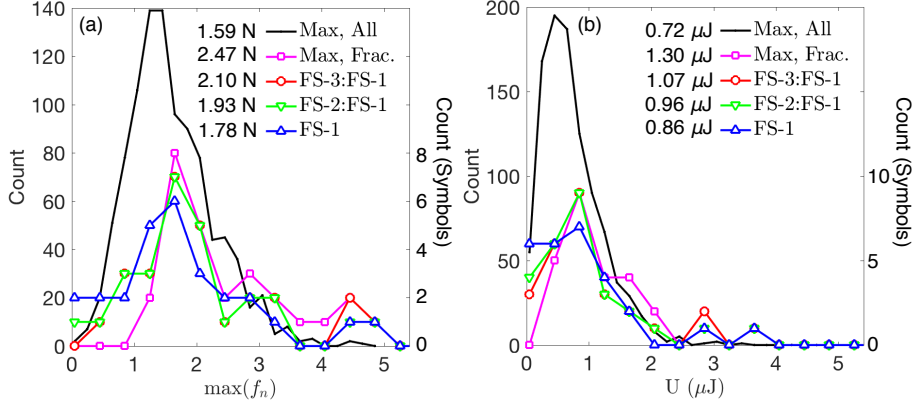


Figure 6: (a) Distributions of the maximum force experienced by all grains (Max, All), fractured grains in the step prior to fracture (FS-1), fractured grains in any of the two steps prior to fracture (FS-2:FS-1), fractured grains in any of the three steps prior to fracture (FS-3:FS-1), and fractured grains at any step (Max, Frac.). (b) Same as (a) but for stored elastic energy,  $U$ . Numbers next to legend entries indicate averages values of  $\max(f_n)$  or  $U$  over corresponding steps.

fracture tend to fracture along planes with a lower total and normalized resolved shear stress than do large grains (normalized  $\sigma_t$  of 0.26 for small grains versus 0.48 for large). Figure 5(b) illustrates this finding on the normalized Mohr's circle. The origin of this difference is not clear and may simply be due to the small sizes of these two populations.

### 3.1.2. The influence of inter-particle forces on fracture

To evaluate the applicability of a maximum inter-particle force fracture criterion, such as the one suggested by [25, 26], we calculated inter-particle forces as described in section 2.4 and [33]. As described in [33], the inferred inter-particle forces are those that best satisfy force equilibrium and the volume-averaged stress measurements for each grain. Normal force magnitudes tend to follow an exponential decay above the mean force at each load step, in agreement with prior experimental and numerical work [48].

We evaluated the maximum normal force on fracturing grains in the step prior to fracture (FS-1), in the two steps prior to fracture (FS-2:FS-1), in the three steps prior to fracture (FS-3:FS-1), and at any step (Max, Frac.) and superimposed these on the maximum forces experienced by all grains at any load step (Max, All) in Fig. 6a. The numbers in the legend are the means of the corresponding distributions. Maximum forces were evaluated on fractur-

ing grains at multiple load steps because it is possible that fractures below the resolution limits of XRCT images caused load drops in the step before fracture was first observed. We observe in Fig. 6a that maximum forces on grains experiencing fracture exhibit a distribution with a slightly higher mean than that of maximum forces experienced by all grains. However, the difference in means of these distributions decreases when the window of steps across which forces are considered narrows to the step immediately prior to fracture, which lends support to the prior suggestions that grains fracture prior to the observation of fractures in XRCT images. Nevertheless, the differences between some of these means and the mean for all grains are statistically significant according to a two-sided Welch’s  $t$ -test as follows: the difference in Max, Frac. is significantly different at the  $> 99.9\%$  confidence level (d.o.f. = 26.5,  $t = 4.49$ ); the difference in FS-3:FS-1 is significant at the 95% confidence level (d.o.f. = 26.5,  $t = 2.41$ ); the difference in FS-2:FS-1 is significant at the 80% confidence level (d.o.f. = 26.6,  $t = 1.62$ ); the difference in FS-1 is not significant at the 80% confidence level. These results suggest that grains experiencing fracture also experience higher inter-particle normal forces than the mean in the steps prior to observed fracture.

To assess whether total elastic energy provides a better predictor of grain fracture than maximum force, we computed the stored elastic energy in each grain,  $U$ , by assuming contact forces approximately follow a Hertzian contact law (this assumption is *not* made in the inference of contact forces [28, 33]. This is similar to the fracture criterion based on average forces used in [49], but employs grain attributes as multiplicative factors when summing forces rather than the multiplicative factors used in that work. We note that we did not use average intra-granular stresses to calculate  $U$ . Positive and negative values in the stress field within individual grains cancel one another’s contribution to the average intra-granular stress, and therefore to any strain energy density computed from the average intra-granular stress. However, the force inference method described in section 2.4 yields accurate inter-particle forces despite this cancellation, because it considers the stresses and equilibrium conditions of adjacent grains. This is evidenced by the accurate forces found in [50], despite the presence of stress fields with positive and negative stress values within individual grains.  $U$  is calculated by

$$U = \sum_{c=1}^{N_c^p} \frac{3}{5(6)^{1/3}} \frac{f_{nc}^{5/3}}{\bar{E}^{2/3} \bar{R}^{1/3}}, \quad (8)$$

where  $N_c$  is the number of contacts on the grain,  $f_{nc}$  is the normal force at contact  $c$ ,  $\bar{E}$  is the harmonic mean of the Young's moduli of contacting surfaces, and  $\bar{R}$  is the harmonic mean of radii of curvature of contacting surfaces. The radius of curvature of all system boundaries was assumed to be infinite. Figure 6(b) shows that stored elastic energies in fracturing grains following the same trends relative to the mean as the maximum inter-particle forces. Similarly, statistical significance is at nearly the same level for each of the differences in means: the difference in Max, Frac. is significant at the  $> 99\%$  confidence level (d.o.f.= 26.5,  $t = 3.65$ ); the difference in FS-3:FS-1 is significant at the 90% confidence level (d.o.f.= 26.4,  $t = 2.05$ ); the difference in FS-2:FS-1 is significant at the 80% confidence level (d.o.f.= 26.5,  $t = 1.48$ ); the difference in FS-1 is not significant at 80% confidence level. As with the inter-particle force results, these results suggest that grains experiencing fracture tend to have higher stored elastic energies than the mean in the steps prior to fracture.

### 3.1.3. Fracture orientations relative to stresses and contact fabric

Fracture planes have been widely observed to align with maximum principal tensile stress, an observation that motivates the use of Brazilian tests [21]. To assess the role of intra-granular stress in *in situ* fracture during multi-contact loading, we computed the dip angles between fracture plane normals and the maximum compressive,  $\sigma_3$ , and tensile,  $\sigma_1$ , principal stress directions. Figure 7(a) illustrates that fracture surfaces exhibit high dip angles relative to  $\sigma_3$  directions, consistent with findings of Brazilian tests [21] and in agreement with the finding that fractures align more closely with the principal tensile stress direction than the principal compressive stress direction. However, Fig. 7(b) shows that fracture surfaces do not necessarily align with the  $\sigma_1$  direction, exhibiting an average dip angle of  $45.3^\circ$  relative to this direction. This finding may reflect the role of the intermediate principal stress,  $\sigma_2$ , on fracture. Mean values of  $(\sigma_1 - \sigma_2)/(\sigma_1 - \sigma_3)$ , reflecting the proximity of  $\sigma_2$  to either  $\sigma_1$  (a value of 0) or  $\sigma_3$  (a value of 1), were 0.65 with a standard deviation of 0.15. As described in [51, 52], the proximity of  $\sigma_2$  closer to  $\sigma_1$  than  $\sigma_3$  increases the likelihood of fracture on planes inclined to  $\sigma_1$ , in agreement with the results of Fig. 7(b). We did not observe a systematic change in strength, or  $\sigma_n$  and  $\sigma_t$  values, with changes in  $(\sigma_1 - \sigma_2)/(\sigma_1 - \sigma_3)$ , like those reported in [51, 52], likely due to the limited number of grain fractures. Nevertheless, these results highlight the complex nature of fracture influenced by the multiaxial stress state within

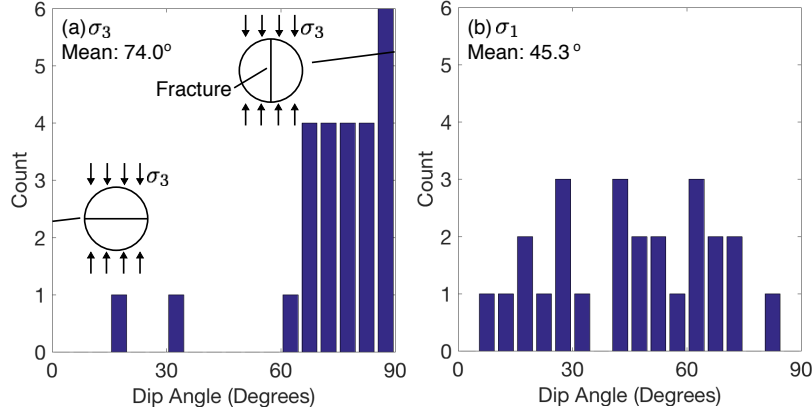


Figure 7: Dip angles of fracture surfaces relative to  $\sigma_3$  (a) and  $\sigma_1$  (b) directions in the step prior to fracture. Insets illustrate conditions at  $0^\circ$  and  $90^\circ$ .

grains experiencing multi-contact loading.

To examine how grains fracture as a function of contact locations, we computed the dip angles between fracture plane normals and the maximum eigenvalue of the fabric tensors  $F_{ij}$ , or  $F_1$ , and the force weighted fabric tensors

$$\tilde{F}_{ij} = \frac{1}{\langle f_n \rangle} \sum_{c=1}^{N_c} f_n n_i^c n_j^c, \quad (9)$$

or  $\tilde{F}_1$ , for each grain, where  $f_n$  is the force at contact  $c$  and  $\langle f_n \rangle$  is the average contact force on the grain. Figure 8(a) suggests that fracture surfaces tend to exhibit high dip angles relative to the maximum eigenvalue of  $F_{ij}$ . An interpretation of what this means in the case of diametrically opposed contact forces is shown in the inset. This trend is similar to, but weaker than, that of Fig. 7(a). The similarity stems from the fact that non-cohesive grains with low inter-particle friction have maximum compressive stress directions similar to the maximum eigenvalue of  $F_{ij}$ . Figure 8(b) shows that the maximum eigenvalue of  $\tilde{F}_{ij}$  has, on average, a higher dip angle to the fracture surface than does the maximum eigenvalue of  $F_{ij}$  in grains that fracture.

The findings of Figs 7 and 8 highlight the complex relationship between intra-granular stress, contacts, and fracture surfaces. They generally suggest that fractures can be used to assess the stress and contact histories of grains that have not significantly rotated after fracturing, a possibility raised in other research [6].

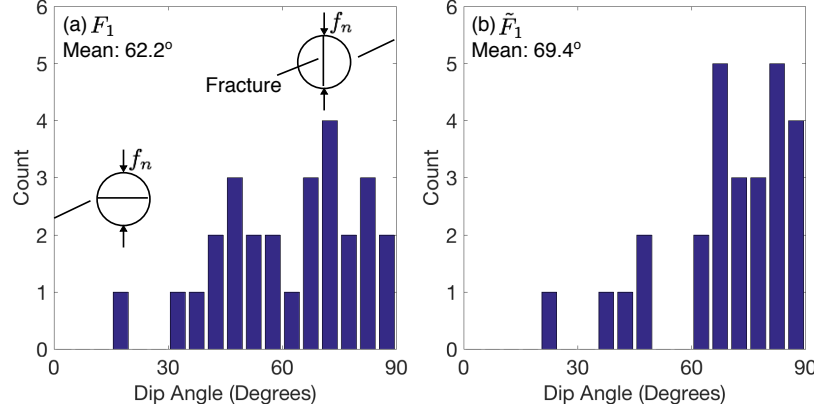


Figure 8: Dip angles between fracture surfaces and (a) unweighted principal fabric,  $F_1$ , and (b) weighted principal fabric,  $\tilde{F}_1$ , directions in the step prior to fracture. Insets illustrate conditions at  $0^\circ$  and  $90^\circ$ .

We used initial coordination number (at step 0),  $Z$ , to assess whether contact number influences grain fracture mechanics, as suggested in [10]. Using initial  $Z$  permits us to compare the population of grains that eventually fracture to the entire grain population, providing a greater chance for a statistically meaningful result than if  $Z$  was compared in specific load steps during which only a few grains fractured. The average initial  $Z$  was 5.26 for grains that eventually fractured and 5.97 for all grains. A two-sided Welch's  $t$ -test confirms that the difference in these two coordination numbers are significant at the 98% confidence level (d.o.f. = 27.56,  $t = -2.50$ ), confirming the suggestion in [10] that an increase in  $Z$  decreases the likelihood of grain fracture.

#### 3.1.4. Fracture orientations relative to lattice planes

We used the crystal plane orientations determined using 3DXRD to assess the influence of crystal plane orientations on fracture plane orientations. Sapphire possesses an anisotropic fracture toughness,  $K_{IC}$ , with values of  $4.54 \pm 0.32$  MPa  $\text{m}^{1/2}$  for the  $c$ -plane,  $3.14 \pm 0.30$  MPa  $\text{m}^{1/2}$  for the  $m$ -plane,  $2.38 \pm 0.14$  MPa  $\text{m}^{1/2}$  for the  $r$ -plane, and  $2.43 \pm 0.26$  MPa  $\text{m}^{1/2}$  for the  $a$ -plane [45]. Accordingly, both slow crack growth and tension testing has found that the  $r$ -plane is the dominant cleavage plane for sapphire [45]. Determining the conditions in which this holds for multi-contact loading could provide insight into when anisotropic fracture models are needed for single-crystal grains in a granular solid under uniaxial compaction.

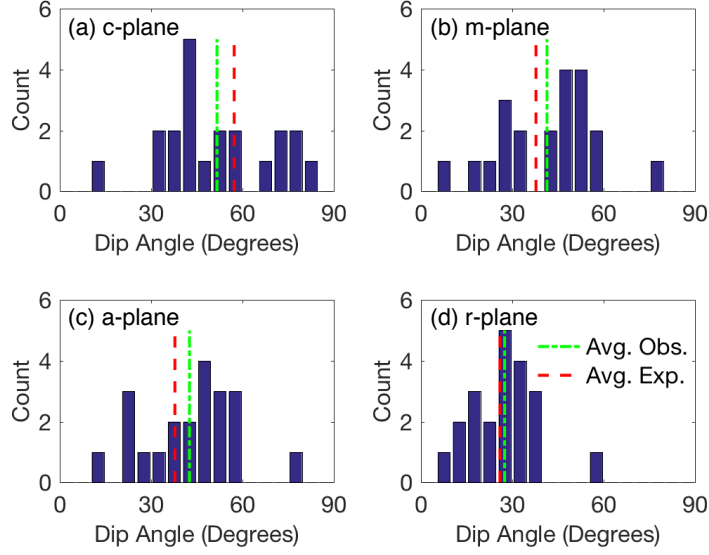


Figure 9: Observed dip angles between fracture planes and the nearest crystal plane, for the *c*- (a), *m*- (b), *a*- (c), and *r*-planes (d). Dot-dashed lines indicate the average dip angles (Avg. Obs.) and the dashed lines indicate the dip angles expected (Avg. Exp.) from randomly oriented fractures.

We computed the dip angle between the fracture plane normal and the *c*-axis, the three-fold *m*-axes, the six-fold *r*-axes, and the three-fold *a*-axes in each grain. For each axis, we retained for analysis only the smallest dip angle for all symmetrically-equivalent axes (e.g., we retained only the smallest dip angle of all six dip angles relative to the *r*-axes). Figure 9 shows the count of dip angles relative to each of the axes. The expected dip angle for a fracture with a random orientation, found by generating  $10^5$  random fracture orientations and performing the procedure just described, are also shown. Fig. 9 suggests that the observed dip angles between fracture planes and crystal planes are the same as would be expected if fracture orientations were entirely random. This has been confirmed by a student's *t*-test, which finds that the dip angles do not differ from those expected from a random distribution at the 80% confidence level. Our data therefore indicates that the effects of intra-granular stress and inter-particle contacts and forces dominate in the determination of fracture plane orientation.

### 3.1.5. Energy associated with grain fractures

The energy dissipation associated with inelastic deformation of granular solids is of broad interest in critical state soil mechanics and plasticity theory (e.g., [7, 12, 53]). Understanding the contribution to energy dissipation from grain fracture would enhance the understanding of how to incorporate fracture into critical state soil models or inelastic constitutive laws for granular materials. We used inter-particle forces to approximate the energy put into, stored in, and dissipated by, the granular solid during compaction. The energy put into the granular solid at a given load step,  $\Delta E$ , was computed by

$$\Delta E = \Delta h \cdot \sum_{c=1}^{N_t} f_n^t \quad (10)$$

where  $\Delta h$  is displacement of the driving piston,  $N_t$  are the number of grains touching the top platen, and  $f_n^t$  are the average normal forces on the top wall, inferred as described in section 2.4 and [28, 33], between the prior step and current step. The energy stored in the granular solid at a given load step,  $U$ , can be determined by summing contributions from each grain in Eqn. (8). The energy dissipated in a given load step can be computed by  $\Delta E - \Delta U$ . Finally, the energy dissipated by the creation of new fracture surfaces,  $E_D$ , can be approximated by assuming the fracture is planar, crosses the center of the grain, and propagates on the nearest  $c$ -,  $m$ -,  $a$ -, and  $r$ -planes for a length proportional to the  $90^\circ$  minus the dip angle to that plane.  $E_D$  takes the form

$$E_D = \pi r_p^2 (Y_f^c m_c + Y_f^m m_m + Y_f^a m_a + Y_f^r m_r) \quad (11)$$

where  $Y_f^c$  is, for instance, the surface energy on the  $c$ -plane and  $m_c$  is  $90^\circ$  minus the dip angle of the fracture normal to the  $c$ -plane, normalized such that  $m_c + m_m + m_a + m_r = 1$ . Values of  $Y_f$  are 40 J/m<sup>2</sup> for the  $c$ -plane, 7.3 J/m<sup>2</sup> for the  $m$ -plane, 6.1 J/m<sup>2</sup> for the  $a$ -plane, and 6.0 J/m<sup>2</sup> for the  $r$ -plane [45]. We note that  $Y_f^a$  was interpolated from the  $m$ - and  $r$ -plane values available in [45] based on  $K_{IC}$  for these planes. Eqn. (11) may overestimate the energy dissipated on the primary fracture surface within a grain but, ultimately underestimates the energy dissipated by the creation of new surfaces since it does not account for secondary fracture surfaces. Future work with XRCT images properly corrected for ring artifacts and using an entire  $180^\circ$  of transmission radiographs (e.g., see [28] that facilitate automatic fragment identification down to several microns would enable a better estimation of



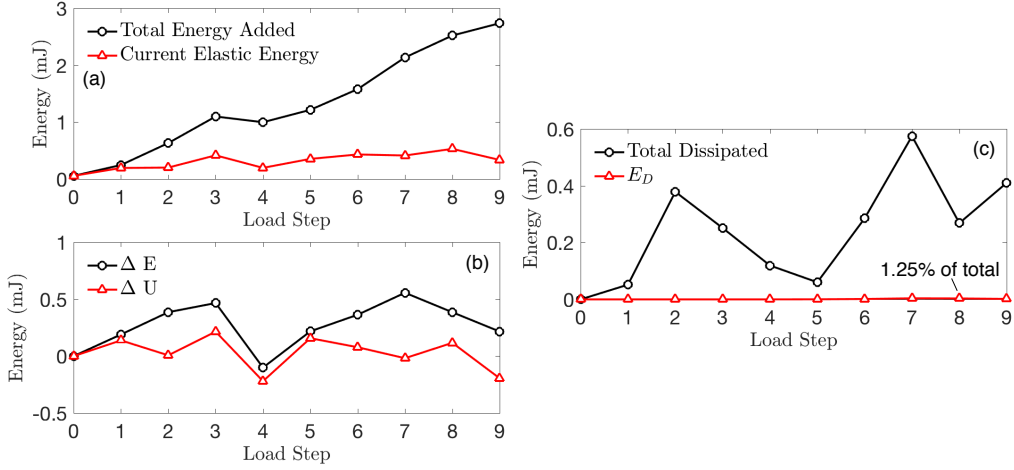


Figure 10: (a) The total energy added to the granular solid and the elastic energy stored in the granular solid at each load step. (b) The change in added energy,  $\Delta E$ , and stored energy,  $\Delta U$ , between each load step and the prior load step. (c) The total dissipated energy, determined from  $U$ , and the energy dissipated by creation of primary fracture surfaces,  $E_D$ .

the energy dissipated by the creation of new fracture surfaces. Nevertheless, our results serve as a reasonable approximation.

Figure 10(a) shows the total energy added to the granular solid, computed at each step by summing the contributions from Eqn. (10) for all prior load steps and the current elastic energy in the granular solid, computed by summing  $U$  from Eqn. (8) for all grains at each load step. Energy is clearly added to the granular solid for all steps except step 4, during which the sample was unloaded as described in section 2. The energy stored in the granular solid, however, remains relatively constant between steps 1-2 and 6-7, and decreases between steps 3-4 and 8-9. The one-step change in these energies is shown in Fig. 10(b). Figure 10(c) shows the total dissipated energy, which is the difference between the two curves in Fig. 10(b). Figure 10(c) also shows  $E_D$ , the approximate energy dissipated by the creation of the primary fracture surfaces during grain fracture. It is clear that  $E_D$  is responsible for a very small portion of the total energy dissipated by the granular solid during compaction. This finding is in agreement with past research [54] and suggests that the true contribution of fracture to energy dissipation during compaction of granular solids may be in the the generation of new internal degrees of freedom that facilitate additional frictional dissipation.

### 3.2. Compaction of Sapphire and Copper

For brevity, we report only select measurements from sample 2, in order to examine the behavior of samples containing phases with difference compliances and ductilities. Sample 2 featured uniaxial compaction of 205 spherical single-crystal sapphire grains, 95 with diameter  $193 \pm 2 \mu\text{m}$  and 110 with diameter  $158 \pm 4 \mu\text{m}$  and 28 copper grains to nearly 30% strain, as described in section 2. During compaction, 66 of the 205 grains fractured between load steps 10 and 19. Figure 11 contains two renderings of the sample at load step 0, one showing all grains and one highlighting grains that fractured. A separate snapshot, taken in the  $x$ - $y$  plane, is also shown for each grain at the first step in which fracture was observed.

#### 3.2.1. The influence of intra-granular stress on fracture

As in the first sample, we computed  $\sigma_h$  and  $\sigma_m$  in the steps immediately prior to fracture and superimposed those states on a density plot of the maximum  $\sigma_h$  and  $\sigma_m$  experienced by all grains. The result in Fig. 12(a) conveys the wide range of stress states experienced by grains that fracture, relative to all grains in the solid. We omitted trajectories of fractured grains in  $(\sigma_h, \sigma_m)$  space for visual clarity.

Sample 2 differs from sample 1 in the following ways. For grains that fracture,  $\sigma_h$  in the step prior to fracture is less than  $\sigma_h$  in grains that do not fracture (mean of 82.4 MPa versus 166.5 MPa) at >99.9% confidence level according to a two-sided Welch's  $t$ -test (d.o.f. = 194.0,  $t = -8.92$ ). This trend was observed but found not to be statistically significant in sample 1. Grains that fracture have  $\sigma_m$  values in the step prior to fracture that are less than those in grains that do not fracture (206.8 MPa versus 301.2 MPa) at the >99.9% confidence level (d.o.f. = 197.0,  $t = -4.89$ ). This last result is in contrast to the findings from sample 1, which found  $\sigma_m$  higher in grains that fractured than the general population of grains. This motivated us to investigate whether the presence of copper in sample 2 affected the fracture response of individual grains, which we discuss in section 3.2.4.

We again used  $\sigma_{ij}$  for each grain with  $\tilde{n}_i$ ,  $t_i^{(1)}$ , and  $\tilde{t}_i^{(2)}$  to estimate  $\sigma_n$  and  $\sigma_t$  on each grain's primary fracture surface. Density maps of  $(\sigma_3, \sigma_s)$  and  $(\sigma_1, \sigma_s)$  are illustrated on the same plot in Fig. 12 and superimposed with the  $(\sigma_n, \sigma_t)$  state of grains in the step before they were first observed to fracture. As with sample one, no clear distinctions between the small and large grain populations can be observed. Similarly, the only observable trend is that a majority of grains that fracture do so on planes with  $\sigma_n$  closer to the

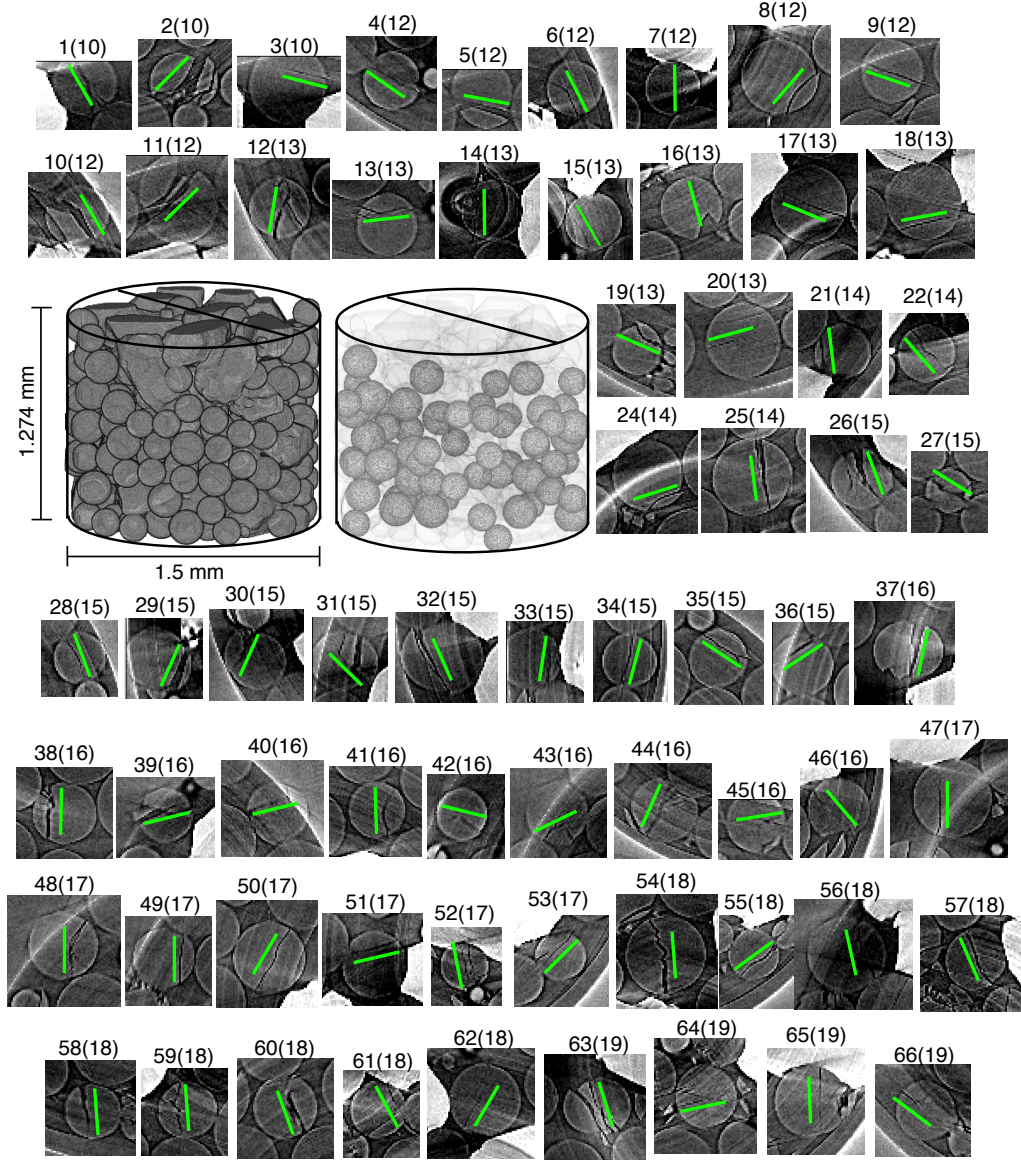


Figure 11: Two renderings of sample 2 at load step 0, one showing all grains and one highlighting those that fracture during sample compaction. A separate figure of each fractured grain, shown in the  $x$ - $y$  plane, is also presented with a green line to guide the reader toward identifying the approximate location of the projection of  $\hat{t}_i^{(2)}$  into the  $x$ - $y$  plane. Figures are labeled by a grain index and load step (in parentheses) indicating the first load step in which fracture was observed. Lines crossing the entire figures are ring artifacts generated during image reconstruction.

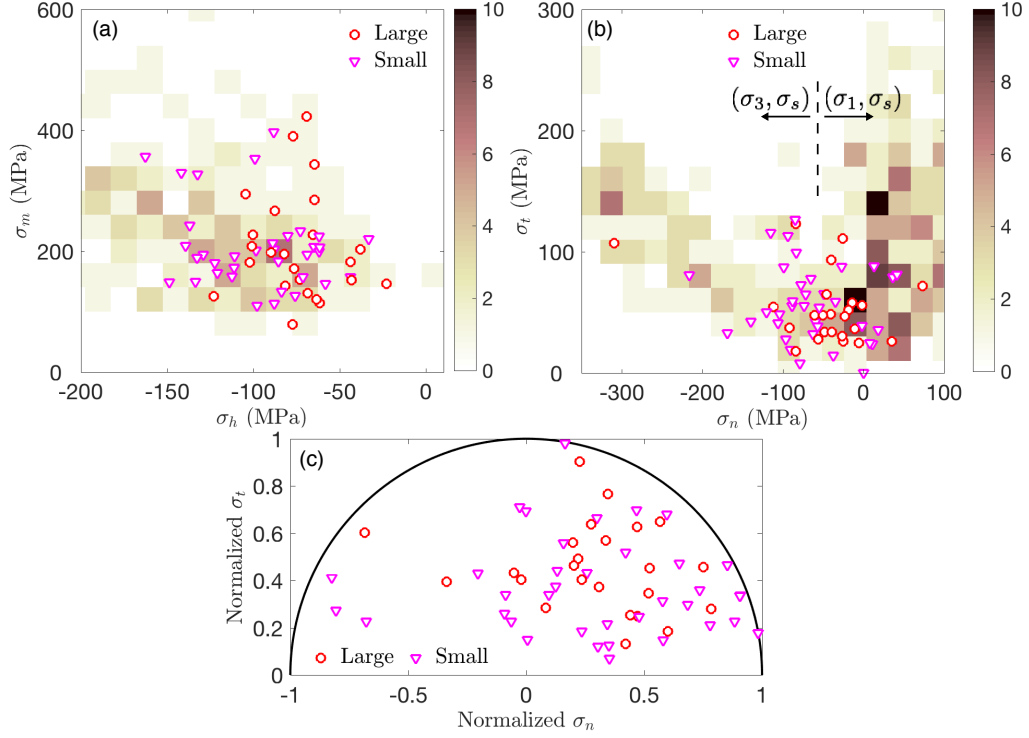


Figure 12: (a) A density map of the minimum and maximum  $(\sigma_h, \sigma_m)$  states for all grains across all load steps, with symbols for grains that fracture representing their state in the step prior to fracture. (b) Density maps of  $(\sigma_3, \sigma_s)$  and  $(\sigma_1, \sigma_s)$  for each grain, where  $\sigma_3$  is the minimum value achieved at any load step during compaction and  $\sigma_1$  is the maximum value achieved at any load step. Also shown are  $(\sigma_n, \sigma_t)$  states of primary grain fracture surfaces in the step immediately prior to the observation of fracture. (c) Normalized Mohr's circle showing normalized values of  $\sigma_n$  and  $\sigma_t$  on the planar fracture surface in each grain that fractures, in the step prior to fracture.

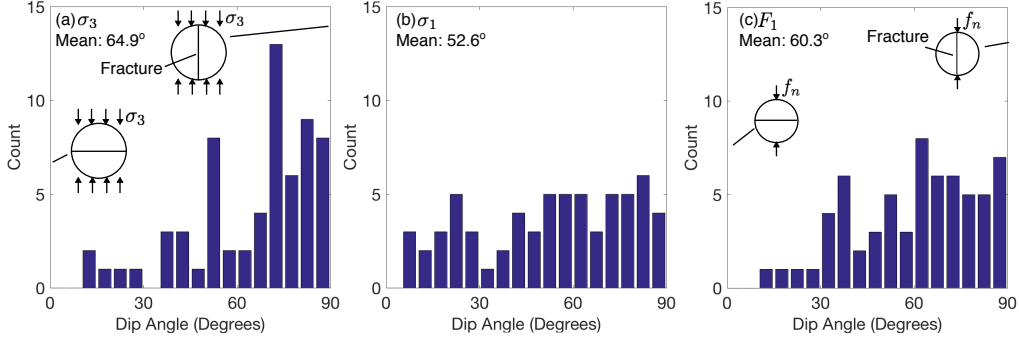


Figure 13: Dip angles of fracture surfaces relative to  $\sigma_3$  (a),  $\sigma_1$ , (b), and  $F_1$  (c) directions in the step prior to fracture. Insets illustrate conditions at  $0^\circ$  and  $90^\circ$ .

maximum tensile stress than the maximum compressive stress in the grain. To corroborate this observation, we again normalized  $\sigma_n$  and  $\sigma_t$  and present them on a single Mohr's circle in Fig. 12c. We observe 48 of the 62 grains with a stress state known in the step prior to fracture to have fractured on planes closer to  $\sigma_1$  than  $\sigma_3$ . The mean normalized  $\sigma_n$  in Fig. 12c is 0.28. This is smaller than the mean normalized  $\sigma_n$  from sample 1, which may reflect a change in the nature of fracture due to the change in sample aspect ratio or the presence of a ductile copper phase.

### 3.2.2. Fracture orientations relative to stresses and contact fabric

We computed dip angles between fracture plane normals and  $\sigma_3$  and  $\sigma_1$  directions. Figure 13(a) shows that fractures exhibit high dip angles relative to  $\sigma_3$  directions, similar to sample 1. Also as in sample 1, fractures do not necessarily align with the  $\sigma_1$  direction and exhibit a  $52.6^\circ$  mean dip angle relative to this direction, as shown in Fig. 13(b). In Fig. 13(c) we show that fractures also exhibit high dip angles relative to the principal eigenvalue of the fabric tensor,  $F_1$ , as shown for the first sample in Fig. 8. The three findings conveyed in Fig. 13 agree with those found for sample 1.

The initial  $Z$  of grains that eventually fractured was 4.94 and was not significantly lower than that of grains that did not fracture (4.92). Although this contrasts with findings from sample 1 and [10], this result may indicate that sapphire-copper contacts, which were included in the calculation of  $Z$ , fundamentally change the fracture mechanics of the sapphire grains. This point is further explored in section 3.2.4.

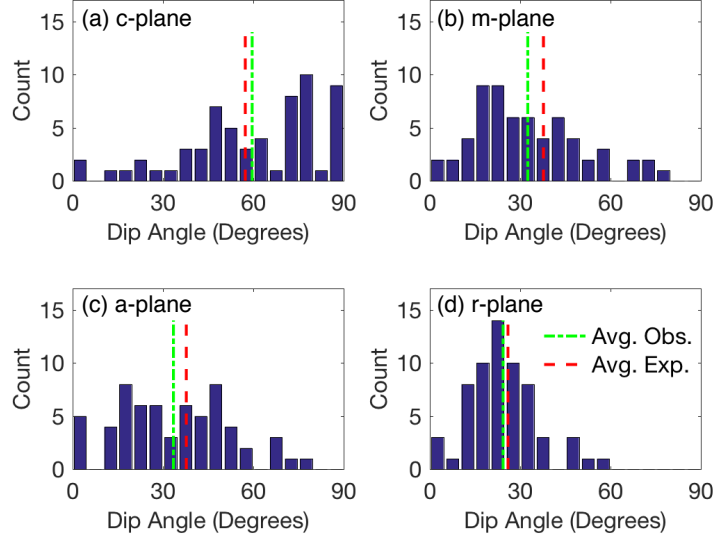


Figure 14: Observed dip angles between fracture planes and the nearest crystal plane, for the *c*- (a), *m*- (d), *a*- (c), and *r*-planes (d). Dot-dashed lines indicate the average dip angles (Avg. Obs.) and the dashed lines indicate the dip angles expected (Avg. Exp.) from randomly oriented fractures.

### 3.2.3. Fracture orientations relative to lattice planes

Our data for sample 2 confirm our claim, from analysis of sample 1, that the orientation of intra-grain crystal planes does not play a dominant role in determining the orientation of primary fracture surfaces in grains. Figure 14 shows the count of dip angles relative to each major crystal plane in the sapphire grains, analogous to Fig. 9 for sample 1. As in that sample, a student's *t*-test confirms that dip angles do not differ from those expected from a random distribution at the 80% confidence level. This further lends evidence to the claim that anisotropic fracture models may not be needed for single-crystal grains (in a granular solid) that possess a similar fracture toughness anisotropy to sapphire.

### 3.2.4. The influence of ductile grains on fracture

Motivated by the difference in fracture behavior as a function of  $\sigma_h$  and  $\sigma_m$  observed in Fig. 4(a) for sample 1 and Fig. 12(a) for sample 2, we investigated whether the presence of copper, a ductile phase relative to sapphire, affected grain fracture. Copper has a Young's modulus of 125 GPa and is known to be ductile [55] while sapphire has a Young's modulus of 380 GPa

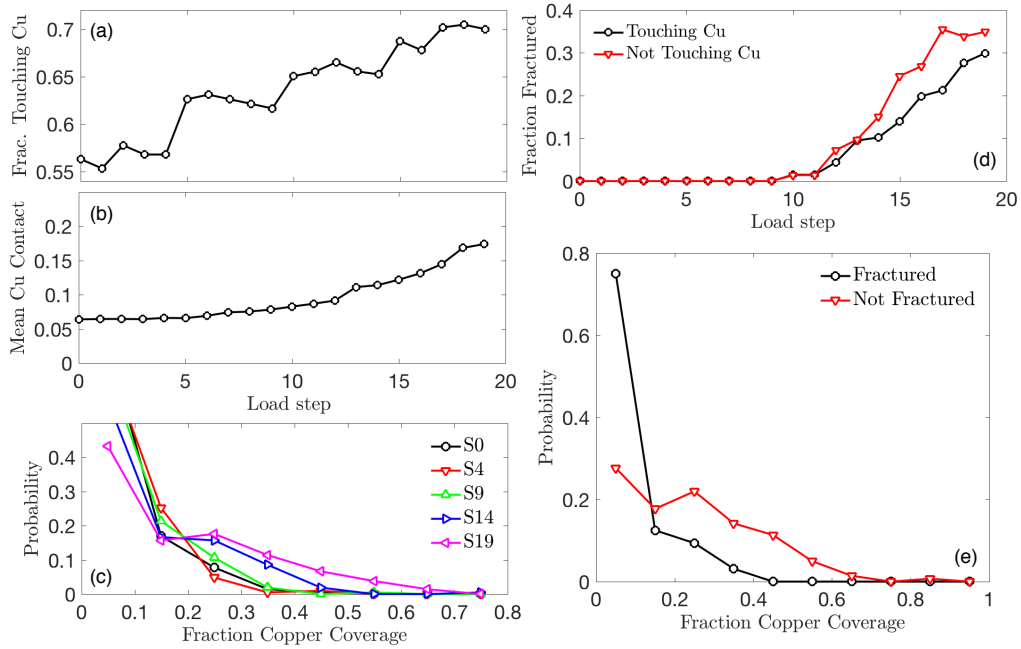


Figure 15: (a) Fraction of grains touching copper in sample 2 as a function of load step. (b) Mean fraction of each grain's surface in contact with copper as a function of load step. (c) Probability distribution of the fraction of each grain's surface in contact with copper at 5 load steps, 0, 4, 9, 14, and 19. (d) The fraction of grains in the population of grains touching, and not touching, copper that are fractured at each load step. (e) Probability distributions for the fraction of copper surface coverage for the populations of grains that are fractured and not fractured.

and is known to exhibit brittle fracture [45]. In fact, during compaction to 30% sample strain, copper is observed to flow through the void space in the sapphire, almost fully enveloping several grains.

Figure 15(a) shows the fraction of sapphire grains that are in contact with copper at each load step, as determined from XRCT images. More than half of the grains are contacting copper prior to the onset of compaction. Figure 15(b) shows the mean fraction of each grain's surface that is in contact with copper at each load step. This calculation includes both grains touching copper and those not touching copper. A monotonic increase is observed in Fig. 15(b), with a slow increase in upward slope after grains begin fracturing in load step 10. Figure 15(c) shows the distribution of the fraction of each grain's surface in contact with copper at load steps 0, 4, 9, 14, and 19. At load step 0, the distribution is sharply skewed toward 0, with almost no

grains having more than 30% of their surface in contact with copper. The distribution widens with load step and at the highest load, nearly a third of all sapphire grains have more than 20% of their surface in contact with copper, with several having more than 60% of their surface in contact with copper.

In Fig. 15(d) we consider two populations of grains: one containing grains touching copper and one containing grains not touching copper. These populations change with load, as indicated in Fig. 15(a). The fraction of grains that fracture is clearly higher in the population of grains not touching copper, suggesting that contact with copper affects a grain’s likelihood of fracture. More striking evidence for this claim can be found by instead considering the population of grains that is fractured by the end of the experiment and the population of grains that is not fractured. In Fig. 15(e) we show the probability distributions for the fraction of copper surface coverage for these two populations. For the population of grains that is fractured during compaction, only the fraction of copper coverage in the load step immediately prior to fracture is considered for each grain. For the population of grains that is not fractured during compaction, the fraction of copper coverage considered when calculating the distribution is taken as the maximum copper coverage at any time during the experiment. Grains that are fractured during sample compaction tend to have very little of their surface in contact with copper in the step prior to fracture. In fact, no grains that fracture have more than 40% of their surface in contact with copper in the step prior to fracture. In contrast, nearly 20% of the population of grains that are not fractured during sample compaction feature surface coverages in excess of 40%. The mean fraction of surface coverage in grains that are fractured, in the step before fracture was first observed, is 0.065. The mean fraction of maximum surface coverage for grains that are not fractured is 0.23. This difference is statistically significant at a >99.9% confidence level according to a Welch’s  $t$ -test (d.o.f. = 121.8,  $t = -11.48$ ). This finding strongly suggests that a ductile secondary phase can alter the fracture mechanics of brittle grains in a granular solid.

#### 4. Discussion

Our results underscore the complex nature of *in situ* grain fracture mechanics during uniaxial compaction of granular solids. A broad range of fracture criteria have been proposed in the literature (e.g., [25, 26, 49]), including



those based on intra-granular stresses and inter-particle forces. We explored the applicability of stress-based fracture criteria during compaction of sapphire spheres by examining the range of average intra-granular stress states that precede grain fracture in both samples. We found the results based on von Mises and hydrostatic stresses to vary between samples which have a diverse compositions. In sample 1 (sapphire only), grains that fractured had above average von Mises stresses,  $\sigma_m$ , and approximately average hydrostatic stresses,  $\sigma_h$ , in the step before fracture. In contrast, in sample 2 (sapphire and copper), grains that fractured had below-average von Mises stresses,  $\sigma_m$ . These results suggest that average intra-granular stresses alone may be insufficient for predicting fracture within individual grains of a granular solid, and that principal stress directions, forces, and contact fabric may also need to be considered. The results based on resolved shear and normal stresses were in agreement across both samples: grains tend to fracture along planes experiencing tensile stress that are more closely aligned with their principal tensile stress,  $\sigma_1$ , than  $\sigma_3$ . These calculations in samples undergoing more significant compaction and fracture may permit assessing the applicability of Weibull’s survival probability by associating  $\sigma_3$  with the characteristic tensile stress,  $\sigma$  (e.g., see [15]). However, the presence of only 27 fracturing grains in sample 1 and less than one-third of grains fracturing in sample 2, makes it challenging to do this with the present data. Future research should focus on assessing Weibull’s survival probability using data similar to that presented here.

We explored the applicability of force-based fracture criteria by examining inter-particle forces that precede grain fracture in the first sample. We found that maximum inter-particle forces, and elastic stored energies computed from these forces, were higher during compaction for grains that fractured than those that did not. This supports the claim that maximum inter-particle force may be used as grain fracture criterion in some granular materials [25, 26, 49]. Since stresses tend to be highest immediately below the surface of inter-particle contacts [25], this criterion is one that considers the maximum local intra-granular stress in samples containing roughly equally-sized spheres. Inter-particle forces tended to drop in the grains that fractured in the steps immediately prior to fracture, possibly indicating the presence of micro-fractures below the resolution limits of XRCT. That several grains also fell below the 3DXRD retention limit in these steps may confirm this possibility. More research should be directed toward determining the range of applicability of an inter-particle force fracture criterion and

more fully understanding the error in the forces inferred by the techniques described in [28, 33].

We explored the nature of fracture orientation by studying the inclination of fracture surfaces to principal intra-granular stresses, contact fabric, force-weighted contact fabric, and lattice planes. This analysis generally showed that a combination of intra-granular stresses and contact fabric control the orientation of primary fracture surfaces. Fracture surfaces within grains in both samples tended to align more closely with  $\sigma_3$  than  $\sigma_1$ , and featured steep dip angles from principal fabric directions (the direction of the eigenvector corresponding to the largest eigenvalue of the fabric tensor). Lattice orientation did not appear to control the orientation of primary fracture surfaces. We therefore can conclude that intra-granular stress and contact fabric are the primary quantities governing the orientation of fracture paths in conditions similar to those tested here. This finding suggests that:

1. grain fracture in geologic soil and rock formations may be used to assess stress histories [6];
2. anisotropic fracture models may not be needed to model single-crystal grains undergoing compaction in a granular solid;
3. there is likely a transition from stress- and contact-dominated fracture orientations to orientations dominated by crystal planes as granular solids become cemented or significantly comminuted, since fractures dominated by crystal orientation are often observed in polycrystalline materials [45].

Point (1) deserves further research, particularly since intra-granular stress and contact fabric appear to be equally important in prescribing fracture surfaces in spheres, but may not be equally important for angular grains, as suggested in [7]. Points (2) and (3) also warrant further investigation since both have important implications for developing and using material models. For point (2), it would be useful for future research to investigate the nature of fracture surfaces on finer length scales, since it is possible that fractures move along preferred cleavage planes in a step-like manner on scales finer than those resolved by XRCT.

We explored the role of grain fracture in *in situ* energy dissipation by computing the amount of energy dissipated by the granular solid due to the creation of the primary fracture surfaces. This energy was found to be very small, approximately 1% of the total dissipated energy, although it may have been underestimated by excluding consideration of secondary

fracture surfaces. Nevertheless, this result is in agreement with past work [54] and suggests that the more important contribution of grain breakage to energy dissipation in granular solids is the unlocking of internal degrees of freedom that enhance frictional dissipation. A specific consideration of this phenomena should therefore be considered in the formulation of breakage models [12].

Finally, we showed through analysis of sample 2 that the presence of a ductile secondary phase can alter the fracture behavior of a granular solid under compaction. It was observed that increased contact with a ductile secondary phase decreased a grain’s likelihood of fracture. This suggests a means for tailoring the microstructure response of a granular solid by modifying the relative ratio of brittle and ductile phases. More research should be performed to understand this result in additional samples and to frame it in the context of effective medium theory.

In the present work, we have not made an attempt to characterize fracture types. Future research should focus on characterizing the various types of fractures as, for instance: cleavage of spherical caps near contacts, fracture through the grain center, planar versus non-planar fracture surfaces, fracture in modes I, II, and III.

## 5. Conclusions

We have presented new experimental insight into the grain-scale aspects of *in situ* grain fracture using XRCT and 3DXRD. This work highlights a new application for these combined x-ray measurements and provides details about grain fracture that have important implications for theory and modeling. Our analyses underscored the complex nature of grain fracture and motivated further research on a broader collection of samples. The results showed that, for granular solids composed of spheres undergoing compaction: (1) average stress states in fracturing grains vary widely compared with grains that do not fracture; (2) fracturing grains experience higher forces and stored elastic energies than intact grains, confirming the applicability of maximum inter-particle force fracture criterion; (3) fracture plane orientations are dominated by intra-granular stress and contact fabric, not crystal plane orientations, making anisotropic grain-fracture models unimportant in un-cemented granular solids under compaction; (4) the creation of new surfaces during fracture has a negligible effect on dissipated energy, and primarily contributes by enhancing frictional dissipation; (5) mixing brittle and

ductile grains may alter which grains are likely to fracture during compaction.

## Acknowledgements

The authors thank Dr. P. Kenesei and Dr. J.-S. Park for help in executing the experiments and Dr. M. A. Homel and Dr. R. Crum for valuable discussions. The authors acknowledge the Advanced Photon Source (APS) for synchrotron beamtime under proposal GUP-45260. Use of APS, an Office of Science User Facility operated for the U.S. Department of Energy (DOE) Office of Science by Argonne National Laboratory, was supported by the U.S. DOE under Contract No. DE-AC02-06CH11357. R.C.H. and E.B.H. acknowledge support from Lawrence Livermore National Laboratory's (LLNL) Laboratory Directed Research and Development (LDRD) program under grant number 17-LW-009. All authors acknowledge support from LLNL's LDRD program under grant number 16-ERD-010. This work was performed under the auspices of the U. S. DOE by LLNL under Contract DE-AC52-07NA27344.

## References

- [1] K. L. Lee, I. Farhoomand, Compressibility and crushing of granular soil in anisotropic triaxial compression, *Canadian geotechnical journal* 4 (1) (1967) 68–86.
- [2] N. Yasufuku, A. Hyde, Pile end-bearing capacity in crushable sands, *Geotechnique* 45 (4) (1995) 663–676.
- [3] W. Lim, G. McDowell, Discrete element modelling of railway ballast, *Granular Matter* 7 (1) (2005) 19–29.
- [4] M. Omidvar, M. Iskander, S. Bless, Response of granular media to rapid penetration, *International Journal of Impact Engineering* 66 (2014) 60–82.
- [5] S. Abe, K. Mair, Grain fracture in 3d numerical simulations of granular shear, *Geophysical Research Letters* 32 (5).
- [6] M. H. Anders, S. E. Laubach, C. H. Scholz, Microfractures: A review, *Journal of Structural Geology* 69 (2014) 377–394.

- [7] G. McDowell, M. Bolton, D. Robertson, The fractal crushing of granular materials, *Journal of the Mechanics and Physics of Solids* 44 (12) (1996) 2079–2101.
- [8] M. Kikumoto, D. M. Wood, A. Russell, Particle crushing and deformation behaviour, *Soils and Foundations* 50 (4) (2010) 547–563.
- [9] D. M. Wood, K. Maeda, Changing grading of soil: effect on critical states, *Acta Geotechnica* 3 (1) (2008) 3.
- [10] G. McDowell, M. Bolton, On the micromechanics of crushable aggregates, *Geotechnique* 48 (5) (1998) 667–679.
- [11] B. O. Hardin, 1-d strain in normally consolidated cohesionless soils, *Journal of Geotechnical Engineering* 113 (12) (1987) 1449–1467.
- [12] I. Einav, Breakage mechanics—part i: theory, *Journal of the Mechanics and Physics of Solids* 55 (6) (2007) 1274–1297.
- [13] W. Weibull, Wide applicability, *Journal of applied mechanics* 103 (730) (1951) 293–297.
- [14] A. Nakata, M. Hyde, H. Hyodo, Murata, A probabilistic approach to sand particle crushing in the triaxial test, *Geotechnique* 49 (5) (1999) 567–583.
- [15] G. R. McDowell, A. Amon, The application of weibull statistics to the fracture of soil particles, *Soils and foundations* 40 (5) (2000) 133–141.
- [16] G. McDowell, On the yielding and plastic compression of sand, *Soils and foundations* 42 (1) (2002) 139–145.
- [17] B. K. Atkinson, Subcritical crack growth in geological materials, *Journal of Geophysical Research: Solid Earth* 89 (B6) (1984) 4077–4114.
- [18] K. Wefers, *Alumina chemicals: science and technology handbook*, The American Ceramic Society, Westerville, Ohio 13.
- [19] M. Rubin, I. Lomov, A thermodynamically consistent large deformation elastic–viscoplastic model with directional tensile failure, *International Journal of Solids and Structures* 40 (17) (2003) 4299–4318.

- [20] J. Clayton, Deformation, fracture, and fragmentation in brittle geologic solids, *International Journal of Fracture* 163 (1) (2010) 151–172.
- [21] J. Jaeger, Failure of rocks under tensile conditions, in: *International Journal of Rock Mechanics and Mining Sciences & Geomechanics Abstracts*, Vol. 4, Elsevier, 1967, pp. 219–227.
- [22] O. Ben-Nun, I. Einav, The role of self-organization during confined comminution of granular materials, *Philosophical Transactions of the Royal Society of London A: Mathematical, Physical and Engineering Sciences* 368 (1910) (2010) 231–247.
- [23] A. K. Turner, F. H. Kim, D. Penumadu, E. B. Herbold, Meso-scale framework for modeling granular material using computed tomography, *Computers and Geotechnics* 76 (2016) 140–146.
- [24] M. B. Cil, K. A. Alshibli, P. Kenesei, 3d experimental measurement of lattice strain and fracture behavior of sand particles using synchrotron x-ray diffraction and tomography, *Journal of Geotechnical and Geoenvironmental Engineering* 143 (9) (2017) 04017048.
- [25] A. Russell, D. M. Wood, M. Kikumoto, Particle crushing in granular assemblies, in: *AIP Conference Proceedings*, Vol. 1145, AIP, 2009, pp. 875–878.
- [26] J. P. de Bono, G. R. McDowell, Particle breakage criteria in discrete-element modeling, *Geotechnique* 66 (12) (2016) 1014–1027.
- [27] Z. Karatza, E. Andò, S.-A. Papanicolopoulos, G. Viggiani, J. Y. Ooi, Evolution of particle breakage studied using x-ray tomography and the discrete element method, in: *EPJ Web of Conferences*, Vol. 140, EDP Sciences, 2017, p. 07013.
- [28] R. Hurley, S. Hall, J. Andrade, J. Wright, Quantifying interparticle forces and heterogeneity in 3d granular materials, *Physical review letters* 117 (9) (2016) 098005.
- [29] B. Zhao, J. Wang, M. Coop, G. Viggiani, M. Jiang, An investigation of single sand particle fracture using x-ray micro-tomography, *Géotechnique* 65 (8) (2015) 625–641.

- [30] Y. Nakata, Y. Kato, M. Hyodo, A. F. HYDE, H. Murata, One-dimensional compression behaviour of uniformly graded sand related to single particle crushing strength, *Soils and Foundations* 41 (2) (2001) 39–51.
- [31] M. Cil, K. Alshibli, 3d evolution of sand fracture under 1d compression, *Géotechnique* 64 (5) (2014) 351.
- [32] B. Zhang, E. B. Herbold, M. A. Homel, R. Regueiro, Particle fracture model and its simulation of shpb experiments on sand, *International Journal for Numerical and Analytical Methods in Geomechanics*.
- [33] R. Hurley, J. Lind, D. Pagan, M. Homel, M. Akin, E. Herbold, Linking initial microstructure and local response during quasistatic granular compaction, *Physical Review E* 96 (1) (2017) 012905.
- [34] S. Hall, M. Bornert, J. Desrues, Y. Pannier, N. Lenoir, G. Viggiani, P. Bésuelle, Discrete and continuum analysis of localised deformation in sand using x-ray  $\mu$ ct and volumetric digital image correlation, *Géotechnique* 60 (5) (2010) 315–322.
- [35] M. Cil, K. Alshibli, 3d assessment of fracture of sand particles using discrete element method, *Géotechnique Letters* 2 (3) (2012) 161–166.
- [36] S. A. Hall, J. Wright, T. Pirling, E. Andò, D. J. Hughes, G. Viggiani, Can intergranular force transmission be identified in sand?, *Granular Matter* 13 (3) (2011) 251–254.
- [37] R. C. Hurley, S. A. Hall, J. Wright, Multi-scale mechanics of granular solids from grain-resolved x-ray measurements, *Proceedings of the Royal Society of London A: In Press*.
- [38] J. Lind, D. C. Pagan, M. C. Akin, In-situ grain-scale micromechanical tracking of particle assemblies under load, *Acta Geotechnica* [Under review].
- [39] <https://www1.aps.anl.gov/Sector-1/1-ID/Infrastructure/Compact-load-frame>.
- [40] J. P. Snyder, Map projections—A working manual, Vol. 1395, US Government Printing Office, 1987.

- [41] D. Boyce, J. Bernier, hexrd: Modular, open source software for the analysis of high energy x-ray diffraction data, Tech. rep., Lawrence Livermore National Laboratory (LLNL), Livermore, CA (2013).
- [42] J. Bernier, N. Barton, U. Lienert, M. Miller, Far-field high-energy diffraction microscopy: a tool for intergranular orientation and strain analysis, *The Journal of Strain Analysis for Engineering Design* 46 (7) (2011) 527–547.
- [43] W. Duan, B. B. Karki, R. M. Wentzcovitch, High-pressure elasticity of alumina studied by first principles, *American Mineralogist* 84 (11-12) (1999) 1961–1966.
- [44] E. R. Dobrovinskaya, L. A. Lytvynov, V. Pishchik, *Sapphire: material, manufacturing, applications*, Springer Science & Business Media, 2009.
- [45] L. D. Hart, E. Lense (Eds.), *Alumina chemicals: science and technology handbook*, American Ceramic Society, 1990.
- [46] B. L. Welch, The generalization of student’s’ problem when several different population variances are involved, *Biometrika* 34 (1/2) (1947) 28–35.
- [47] F. E. Satterthwaite, An approximate distribution of estimates of variance components, *Biometrics bulletin* 2 (6) (1946) 110–114.
- [48] T. S. Majmudar, R. P. Behringer, Contact force measurements and stress-induced anisotropy in granular materials, *Nature* 435 (7045) (2005) 1079–1082.
- [49] O. Ben-Nun, I. Einav, A refined dem study of grain size reduction in uniaxial compression, in: *Proceedings of the 12th international conference of the international association for computer methods and advances in geomechanics (IACMAG)*, Goa, India, 2008, pp. 702–708.
- [50] R. Hurley, K. Lim, G. Ravichandran, J. Andrade, Dynamic inter-particle force inference in granular materials: Method and application, *Experimental Mechanics* 56 (2) (2016) 217–229.
- [51] K. Mogi, Effect of the intermediate principal stress on rock failure, *Journal of Geophysical Research* 72 (20) (1967) 5117–5131.



- [52] E. Fjær, H. Ruistuen, Impact of the intermediate principal stress on the strength of heterogeneous rock, *Journal of Geophysical Research: Solid Earth* 107 (B2).
- [53] I. Einav, Breakage mechanics—part ii: Modelling granular materials, *Journal of the Mechanics and Physics of Solids* 55 (6) (2007) 1298–1320.
- [54] M. Bolton, Y. Nakata, Y. Cheng, Micro-and macro-mechanical behaviour of dem crushable materials, *Géotechnique* 58 (6) (2008) 471–480.
- [55] A. I. H. Committee, *ASM handbook: Materials selection and design*, Vol. 20, CRC Press, 1997.